Carbon 169 (2020) 395–402

Contents lists available at ScienceDirect

Carbon

journal homepage: www.elsevier.com/locate/carbon

Optimization of fluorescence and surface adsorption of citric acid/ethanolamine carbon nanoparticles for subsurface tracers

Laura Sinclair [a, *, 1], Joseph Brown [a, b, 1], Muhammad G. Salim [c], Daniel May [d], Bahareh Guilvaiee [e], Adam Hawkins [d], Lawrence Cathles [d]

[a] Robert F. Smith School of Chemical and Biomolecular Engineering, Cornell University, Ithaca, NY, USA
[b] Department of Chemistry, Massachusetts Institute of Technology, Cambridge, MA, USA
[c] Cornell Center for Materials Research, Cornell University, Ithaca, NY, 14853, USA
[d] Department of Earth and Atmospheric Sciences, Cornell University, Ithaca, NY, USA
[e] Department of Biological and Environmental Engineering, Cornell University, Ithaca, NY, USA

ARTICLE INFO

Article history:
Received 3 March 2020
Received in revised form
27 May 2020
Accepted 10 July 2020

ABSTRACT

The tunable fluorescence and biocompatibility of fluorescent carbon nanoparticles (FCNs) makes them appealing tracers in geothermal, environmental, and clinical applications. Here, we address FCNs synthesized from reaction and pyrolysis of citric acid and ethanolamine. We examine the fluorescence and the adsorption of these FCNs as critical parameters that influence their use in applications. FCN fluorescence was observed to develop during pyrolysis and measured at pyrolysis temperatures ranging from 190 to 250 °C. Transmission electron microscopy shows that the FCN average diameter of approximately 13 nm is unaffected by pyrolysis temperature. However, pyrolysis temperature strongly affects fluorescence, which peaks at 210 °C. The surface hydrophobicity of the FCNs increases with pyrolysis temperature as measured by retention on reverse phase chromatography. Together, these results suggest that particle surface functionalities provide both fluorescence and hydrophilicity, and that these surface functionalities are destroyed with excessive pyrolysis. To examine their surface adsorption, quartz crystal microbalance measurements demonstrate that pyrolysis temperature increases FCN adsorption on mineral surfaces. Surfaces with greater hydrophobicity show greater FCN adsorption. Adsorption is unaffected by the presence of mono- or divalent ions in solution. This suggests adsorption by hydrophobic interaction for the Fe_2O_3, SiO_2, and AlSiO surfaces studied.

1. Introduction

Fluorescent carbon nanoparticles (FCNs) have garnered significant attention in the past decade due to their unique optical properties, ease of synthesis, and biological and environmental compatibility. [1–5] Their optical properties include excitation-dependent emission, high photostability, and high quantum yield, on par with other nanomaterials produced using semiconductor materials (e.g., quantum dots) [3,6]. Benefiting from their quick synthesis and desirable properties, FCNs have been employed in biological sensing and imaging, demonstrating their low toxicity and biocompatability [2,3,7,8]. The fluorescent, nanoscale graphitic carbon typically found in FCNs can be prepared through physical or chemical methods [2]. Chemical approaches encompass a wider diversity of methods including oxidation of soot [9,10], electrochemical methods [11,12], and treatment of graphitic carbon (e.g., graphene, graphite) [13–15]. One of the most accessible chemical methods to produce FCNs is through pyrolysis or carbonization of carbon sources, which have varied in complexity from molecular approaches [16–19] to polymeric biomaterials [20–22]. Some have shown impressive quantum yields up to 60% [18,19,23,24]. Of these approaches, the pyrolysis of citric acid with other molecular precursors has emerged as an inexpensive and scalable manner to produce FCNs [4,16,18,19,23–25].

One emerging application for FCNs has been their use as nanoparticle tracers in the characterization and diagnosis of subsurface fluid transport [26–31]. Tracers can be used in inter-well flow experiments to determine the residence time distribution of flow, to approximate porosity, or to identify channeling events

* Corresponding author.
E-mail address: lks82@cornell.edu (L. Sinclair).
[1] These authors contributed equally.

https://doi.org/10.1016/j.carbon.2020.07.024
0008-6223/

[30,31]. These flow regime properties have important implications for heat transfer, diffusional exchange, or chemical reaction rates. Overall, understanding these properties in groundwater systems is important for many applications including oil and gas, geothermal energy, environmental remediation, and in situ leaching [30,32,33]. Ionic tracers such as bromide and chloride salts, deuterated water, and molecular species such as aromatic acid derivatives have been commonly employed [34,35]. However, diffusion of these tracers into non-flowing or "stagnant" fluid-filled regions can lead to significant misinterpretations of the residence time of flow [36,37]. Further complicating matters, halide tracers may undergo ion exchange reactions with clays and other minerals [33,38,39].

Nanoparticles (e.g., FCNs) have limited diffusion into stagnant pores due to their larger size, and therefore hold significant potential as conservative tracers for groundwater systems [31,40,41]. However, the development of noninteracting conservative tracers is challenging as most nanoparticle formulations adsorb to subsurface structures, which can complicate their breakthrough curve and use for the analysis of subsurface flow [26,30,37,38,42]. Adsorption to mineral surfaces can also be difficult to decouple from the stability of the FCNs (i.e., resistance to agglomeration), as both are affected by pH and ionic strength of the media [43,44].

FCNs synthesized from citric acid and ethanolamine are unique because of their low adsorption to mineral surfaces and high stability under various temperature and salinity conditions in comparison to other nanoparticles [26]. Researchers have evaluated several nanoparticle tracer formulations showing varying degrees of stability and inert transport including functionalized silica [45], paramagnetic iron-oxide [46], titanium oxide [47], and fullerene nanomaterials [48]. Previously, multiple FCN formulations were contrasted by measuring adsorption on calcite in various brine compositions. When divalent salts are present, patches of calcite surfaces become positively charged [27]. For some types of nanoparticles (including silica and malic acid/ethanolamine FCNs) this can result in significant retention on calcite surfaces. However, the formulation studied here (citric acid/ethanolamine FCNs) were found to have remarkably little retention on calcite matching the conservative bromide tracer in column retention tests, even with high concentrations of monovalent or divalent salts [26]. This stands in contrast to the adsorption of FCNs prepared with ethylene diamine, which likely carry some residual positive charge and pH dependence, even though they achieve higher brightness and quantum yield (QY) [26,37].

Low adsorption of citric acid/ethanolamine FCNs has also been shown in the field. Remarkably minimal adsorption was observed in a in a major field test carried out at the Ghawar reservoir. The FCNs were slightly less retained than the best inert (not-adsorptive) chemical tracers when deployed in a >2 year test between wells 400 m apart at >100 °C in the carbonate Ghawar field in Saudi Arabia [28,29,49]. These FCNs also proved to be non-adsorptive in several smaller scale field tests in silicate rocks. They performed equivalently to bromide and chloride tracers in all the field tests we have carried out in silicate formations [38,39].

However, this promising work has suffered from a lack of fundamental understanding of the mechanism behind interaction with mineral surfaces. This understanding could lead to further optimization of FCN surface properties to produce ideal nanoparticle tracers. To minimize subsurface adsorption, the nanoparticle surface properties need to be considered. Previous work has demonstrated that size, charge, and hydrophobicity are key parameters that dictate the nanoparticle interaction with proteins, membranes, and other interfaces [50–53]. The minimal adsorption of critic acid/ethanolamine FCNs has been previously attributed to their near neutral surface charge (ζ-potential near zero), small size, and highly hydrophilic decoration of the particles (see Table S1 for compiled properties) [26–29]. However, nanoparticle surface hydrophobicity has also been seen to strongly influence these interactions, increasing protein adsorption [54–56] and immune modulation [57–59]. Thus, researchers have developed generalizable methods to characterize nanoparticle hydrophobicity to further understand and quantify its impact on function [60–62]. The characterization of nanoparticle surface hydrophobicity thus appears as an important parameter to limit their interfacial interactions with mineral surfaces. While our goal is to optimize these nanoparticles for inert subsurface transport, our methods for understanding and tuning surface interactions can be used in other applications including environmental remediation [63–65].

Here, we seek to further optimize citric acid/ethanolamine FCNs by minimizing their adsorption on various mineral surfaces, and also to investigate particle fluorescence and particle size as controlled by pyrolysis temperature [16]. Prior investigation indicated that a lower temperature pyrolysis provided stronger fluorescent brightness by quantum yield compare to other formulations, which we will expand upon [16]. Citric acid/ethanolamine FCNs are synthesized at multiple pyrolysis temperatures from the same ethanolamine and citric acid precursor. After careful dialysis, the spectral properties are measured to determine the pyrolysis temperature that maximizes fluorescence. As nanoparticle surface charge has already been quantified to be neutral, measurement of nanoparticle surface hydrophobicity was completed by reverse-phase high-performance liquid chromatography, showing increased nanoparticle hydrophobicity with pyrolysis temperature. The increases in surface hydrophobicity correspond to increases in nanoparticle adsorption measured by a quartz crystal microbalance with dissipation monitoring (QCM-D). The adsorption is greater on more hydrophobic surfaces. The FCN adsorption is thus due to hydrophobic interactions between the nanoparticles and the surface. Overall, this work demonstrates that many properties of fluorescent carbon nanoparticles are related to their synthetic process parameters, which can lead to their optimization as subsurface nanoparticle tracers. Our results also apply beyond nanoparticle tracers, illustrating how nanoparticle fluorescence and hydrophobicity can be both tuned and characterized.

2. Materials and methods

2.1. Preparation of fluorescent carbon nanoparticles (FCN)

The synthesis procedure from Krysmann 2012 was replicated [16]. Citric acid monohydrate (Sigma Aldrich) was combined with ethanolamine (EMD Millipore) in a 1:3 M ratio as a neat mixture in a round bottom flask. The flask was heated in a round bottom mantle with a temperature controller. An air-cooled reflux condenser was attached to condense any evaporating ethanolamine. The round bottom flask was stirred at 160 °C for 30 min (~5 min of heat-up time), during which the reaction turned bright yellow and then brown. The impure glassy yellow-brown liquid was highly water soluble and will be referred to as the precursor (see Fig. 1). Several grams of the precursor were pyrolyzed in a glass beaker in a preheated atmospheric pressure oven at various temperatures (190 °C, 210 °C, 230 °C, or 250 °C) for 2 h. The dark, solidified material was cooled, dissolved in a minimal amount of deionized water, and dialyzed against deionized water to remove small molecules (Snakeskin, 3.5 kDa MWCO) [4,16]. The dialysis was performed for approximately 1 week with the water changed at least every 24 h, and terminated when minimal fluorescence was detected in the dialysate. The nanoparticles were then lyophilized for at least 48 h, resulting in a light fluffy solid that was sealed in a desiccator to prevent re-hydration.

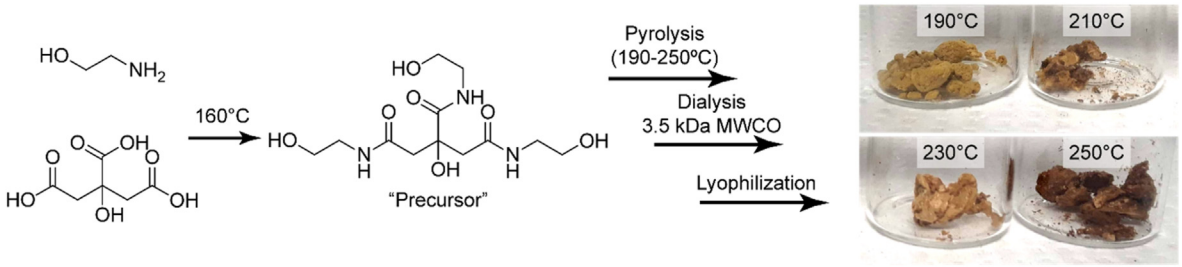

Fig. 1. Synthetic scheme used to form the precursor through the condensation of citric acid and ethanolamine at 160 °C. The precursor was then pyrolyzed across a variety of temperatures, dialyzed, and lyophilized to obtain the light, fluffy, solid fluorescent carbon nanoparticles illustrated. (A colour version of this figure can be viewed online.)

2.2. High performance liquid chromatography (HPLC)

HPLC was used to characterize the hydrophobicity of the particles and the precursor from their retention on reverse phase (C18) silica. HPLC was performed on an 1100 Series Agilent HPLC system using a reverse phase Agilent Eclipse Plus C18 column (4.6 × 150 mm, 5 μm) at 40 °C. Solvents for HPLC were water with 0.1% trifluoroacetic acid (solvent A), and acetonitrile with 0.1% trifluoroacetic acid (solvent B). Compounds were eluted using a standardized gradient of 3.17 %B/min at 1 mL/min, starting at 5% AcN ramping to 100% in 30 min.

2.3. Quartz crystal microbalance with dissipation monitoring (QCM-D)

A mineral crystal sensor chip of specified composition (SiO_2, Fe_2O_3, or AlSiO from Q-Sense, Sweden) was cleaned in UV-Ozone Procleaner (Bioforce, USA) for 20 min to remove any organic contamination and then loaded into a quartz microbalance with dissipation monitoring (Qsense E1, Biolin Scientific, Stockholm, Sweden). The sensor chip was then equilibrated and autotuned under flow of either water or saline solution (50 mM NaCl or 50 mM $CaCl_2$) using a peristaltic pump (Ismatec Reglo Digital M2-2/12, Q-Sense, Switzerland) at 100 μL/min. Once equilibrated, samples were injected and flowed across the sensor chip and the signal response was collected. After each run, the sensor chip was cleaned by sonicating in 2% sodium dodecyl sulfate for 20 min, rinsing thoroughly with water, and drying with nitrogen. Duplicate runs were collected for all conditions shown. FCN adsorption was calculated using the Sauerbrey relation for rigid films [66].

3. Results and discussion

Fluorescent carbon nanoparticles (FCN) were prepared from citric acid and ethanolamine as previously described [16]. The condensation of ethanolamine and citric acid at 160 °C as a neat mixture produced the "precursor," which was examined by ^{1}H and ^{13}C nuclear magnetic resonance (NMR) as well as liquid chromatography mass spectrometry (LCMS). The precursor predominantly consisted of the triamide product of the condensation, with some of the diamide product detected by LCMS (see Figs. S1, S2, and S5). An additional product was also observed from the reaction that matches an additional loss of water and ethanol in an intramolecular condensation from the triamide product. This result suggests that additional condensation reactions can occur in the precursor preparation process.

The precursor was pyrolyzed across a range of temperatures from 190 °C to a maximum of 250 °C (Fig. 1), dialyzed, and lyophilized. These pyrolysis temperatures were chosen because previous investigation indicated higher fluorescence was observed around 230 °C, lower than some other formulations [16]. As previously reported, dialysis is crucial for "bottom-up" synthesis of FCNs to remove highly-fluorescent small molecule contaminants from the nanoparticles in the mixture [4]. The mass yield was assessed and found to be 2%, 4%, 7%, and 26% for the 190 °C, 210 °C, 230 °C, and 250 °C pyrolysis conditions, respectively. These relatively low yields indicated significant removal of smaller particles or unreacted small molecules during dialysis. The mass yield increases with pyrolysis temperature, which is in agreement with a pyrolysis mechanism of molecular agglomeration and polymerization via imide bonding, forming structures large enough to be retained during dialysis [16].

Upon synthesis, the FCNs were characterized for their size and dispersity by transmission electron microscopy (TEM). The images were analyzed using the Image J program to obtain particle size distributions for each pyrolysis temperature. At least 70 particles at each pyrolysis temperature were analyzed, using between three and five images. The particle sizes were not statistically different from each other; all centered at approximately 13 nm diameter, with a significant right skew to the distribution (Fig. 2A). This is in general agreement with previous work, which reported mean particle size of 19 nm for this formulation [16]. Dynamic light scattering (DLS) to determine particle size was attempted, but the carbon nanoparticles demonstrated weak scattering that was insufficient to analyze, even at higher nanoparticle concentrations. Raw correlograms are included the Supporting Information (Fig. S7) indicating the increases in sample concentration reduced the construction of the correlogram, likely indicating strong sample absorbance. Thus, ζ-potential measurements of the FCNs were not readily made, though previous work has shown them to be near-neutral with a reported surface charge of −1.5 ± 2.0 mV and −0.88 ± 3.4 mV in DI water at pH 7.35 and in 2.21 M NaCl, 0.74 M $CaCl_2$, 0.18 M $MgCl_2$ pH 6.34, respectively [26,37]. Nevertheless, all pyrolysis temperatures yielded gram quantities of final fluorescent carbon nanoparticles of the expected size (~13 nm).

Since this formulation of fluorescent carbon nanoparticles (FCNs) has previously demonstrated low mineral surface adsorption [26], attention was first drawn toward understanding more about the fluorescence mechanism. First, the FCNs were analyzed for their absorbance and fluorescence. Excitation and emission curves of the FCNs demonstrated an emission maximum at 466 nm best excited at 376 nm (Fig. S8). A working concentration range was determined where the fluorescence was observed to have a linear response (Fig. S9). With these basic parameters, the precursor was examined in detail by reverse phase HPLC with an in-line absorbance and fluorescence detector (Fig. 3A). This examination revealed that a major peak in absorbance at 230 nm appearing at 3.5 min had little to no fluorescence. Other smaller peaks observed by absorbance at 230 nm had significantly higher fluorescence. This result suggests that the triamide product in the precursor is nonfluorescent, and that pyrolysis was necessary to develop the fluorescence of the FCNs. For further verification, the peak within

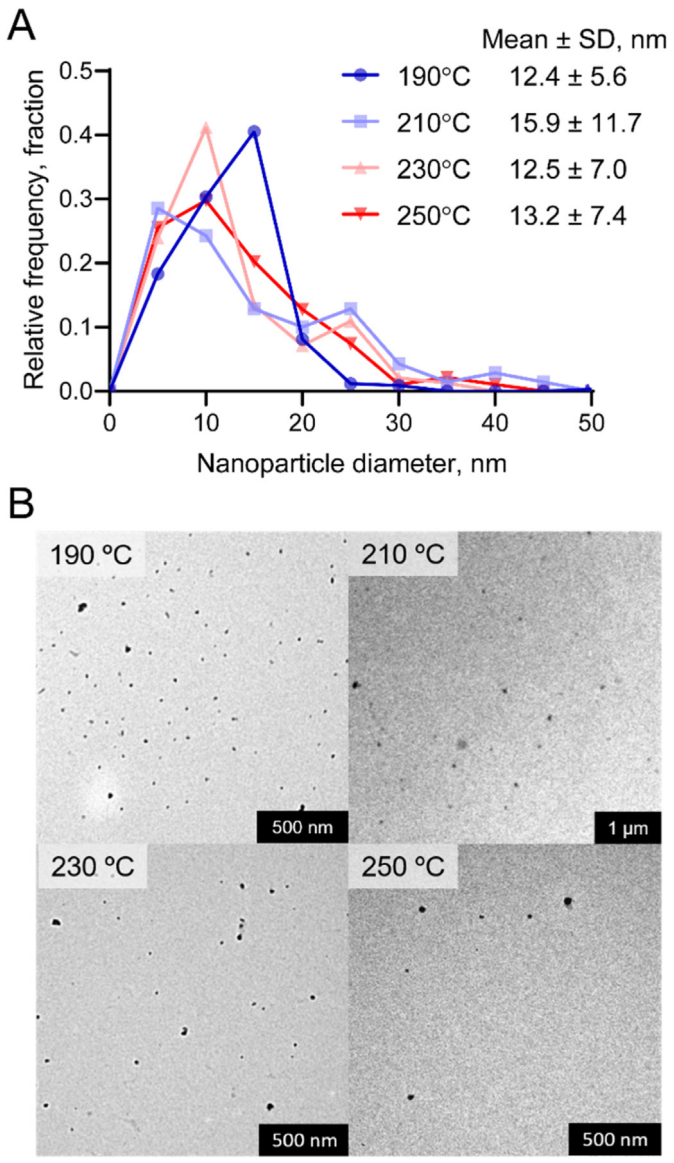

Fig. 2. A. FCN size distribution as revealed by analysis of **B.** transmission electron microscopy images. Multiple images were compiled for analysis such that n = 333, 70, 238, and 94 nanoparticles were analyzed from the 190 °C, 210 °C, 230 °C, and 250 °C pyrolysis conditions, respectively. (A colour version of this figure can be viewed online.)

the green shaded area was collected and analyzed by ^{1}H NMR (Figs. S3 and S4) and also for its fluorescence. This verified that the triamide product and diamide product were nonfluorescent (Fig. 3B).

Fluorescence intensity of the nanoparticles increased with pyrolysis temperature up to a peak at 210 °C (Fig. 3B). However, at a pyrolysis temperature of 230 °C and above, fluorescence intensity dropped dramatically. This intensity tracked well with the quantum yield determined to be 11%, 16%, 10%, and 4% for 190 °C, 210 °C, 230 °C, and 250 °C, peaking at modest pyrolysis temperatures and matching literature reports for this formulation (see Table S1). A similar transition is also observed in the broadness of the absorbance curves of the FCNs seen in Fig. 3C. Specifically, a narrow absorption band appears at 342 nm within the FCNs produced at 190 °C and 210 °C that is only weakly observed in the precursor and not at all in the purified diamide/triamide product. This absorption band is then abolished at pyrolysis temperatures of 230 °C and above, coinciding with the decrease in fluorescence. The absorption spectra broadening at these high pyrolysis temperatures suggests diversification of absorptive functional groups. Also, there is a slight redshift of the fluorescence emission as the pyrolysis temperature increases, in agreement with previously reported observations [16]. The peak emission wavelength was approximately 465 nm for the 190 °C particles and was shifted to approximately 475 nm for the 250 °C particles, though this shift was small relative to the peak width (Fig. S8).

During pyrolysis, the additional energy can drive further chemical reactions (e.g., condensation). The presence of amide and imide groups originally observed by Krysmann et al. [16] was supported by FTIR in all FCN species (Fig. S10). Further condensation can produce the π-conjugated systems common to fluorescent species, similar to the development of citrazinic acid derivatives in other FCN formulations. [5,19,24,67] If the pathway suggested by Song et al. [67] is followed, an additional condensation step will provide an unsaturated ring. Examination of the precursor LCMS revealed that an additional product can be identified that has undergone an intramolecular condensation within the precursor mixture, removing water and ethanol (Fig. S5). However, while it could have developed fluorescent species, the pyrolysis can also lead to the carbonization of the FCN species evolving volatile electronegative functional groups such as ammonia and carbon dioxide. Also, fluorescence of FCNs can arise from multiple edge or surface trapped states of the core graphitic carbon, possibly comprising multiple absorptive states [16,68–70] that appear as broadening in the absorption spectra in Fig. 3C. Additionally, the broadening of absorbance spectra matches the darkening of FCNs themselves as seen in Fig. 1. X-ray photoelectron spectroscopy (XPS) of the precursor and samples provided further insight into the elemental analysis of the FCNs. The carbon content of the FCNs steadily increased with pyrolysis temperature while oxygen content decreased, as observed in both survey scan data and deconvoluted spectra (Figs. S11 and S12). Nitrogen content remained relatively constant from precursor to 250 °C. This additionally supports the loss of electronegative nitrogen and oxygen groups as pyrolysis increases. Overall, the fluorescence maximum at 210 °C may be attributed to the optimal development of fluorescent surface groups with pyrolysis. The XPS data also captures the coinciding buildup of carbogenic species, which increase with further pyrolysis, but are less fluorescent than the fluorophores. Overall, these data suggest that the fluorescence for this FCN formulation is created optimally at 210 °C and then diminished under harsher pyrolysis conditions.

The pyrolysis temperature clearly affects the FCN fluorescence properties, likely through changes in chemical composition. In turn, the pyrolysis temperature can be expected to affect the nanoparticle surface properties, which could affect their adsorption on mineral surfaces. As mentioned, nanoparticle surface hydrophobicity is a key modulator of the nanoparticle interface, affecting protein adsorption [54–56] with broader implications as hydrophobicity continues to be understood and engineered at inorganic interfaces [52,53,71]. Several methods were available generally including the measurement of partition coefficients of either adsorbed fluorophores (e.g., Rose Bengal) or of the FCNs themselves [60]. However, fluorescence measurements might not represent the nanoparticle partitioning well if the nanoparticles are heterogeneous. If the molecular fluorophores suspected from the spectral data were hydrophilic, then the partition would skew toward the hydrophilic phase. Recently, researchers have been able to directly quantify nanoparticle surface hydrophobicity, though the creation of engineered surfaces is required [61,62]. Additionally, chromatographic methods have been explored to examine FCNs by reverse

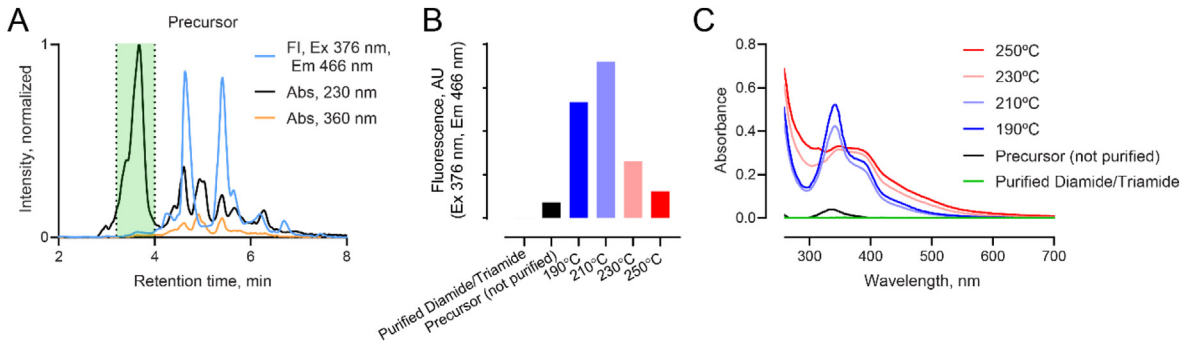

Fig. 3. A. High performance liquid chromatography (HPLC) with in line absorbance and fluorescence detection of the precursor utilizing a C18 reverse phase analytical column. The major peak was collected within the green shaded area and also analyzed by ^{1}H NMR (see Figs. S3 and S4). **B.** The fluorescence intensity at the peak emission of 466 nm versus pyrolysis condition including the precursor and the diamide/triamide product purified from the precursor via HPLC as shown in Fig. 3A. **C.** The absorbance curves of all species. All species in **B.** and **C.** were observed in deionized water at room temperature at FCN concentrations of 0.05 mg/mL for their absorbance and fluorescence, which was within the linear regime of the fluorescence response. (A colour version of this figure can be viewed online.)

phase [72,73] and anion exchange [74], which can quickly examine the entire nanoparticle population with standard analytical methods. Arguably, modern analytical chromatography columns should provide reproducible engineered surfaces, though a fundamental understanding of their retention and elution has not yet been achieved [61,62].

Inspired by these methodologies, we investigated nanoparticle surface hydrophobicity by retention on reverse phase (C18) HPLC (Fig. 4A). The fluorescent carbon nanoparticles were retained more than the precursor itself. Moreover, the FCNs showed greater retention as the pyrolysis temperature was increased, suggesting that the FCNs produced at higher temperature (e.g., 230 °C and 250 °C) have a more hydrophobic surface. Coupled with the spectral results discussed previously (Fig. 3), this also indicates that the functional groups that help produce the FCN fluorescence are likely hydrophilic. As the pyrolysis continues, functional groups that carbonize to evolve off ammonia or carbon dioxide and elemental carbon coincide with increased hydrophobicity.

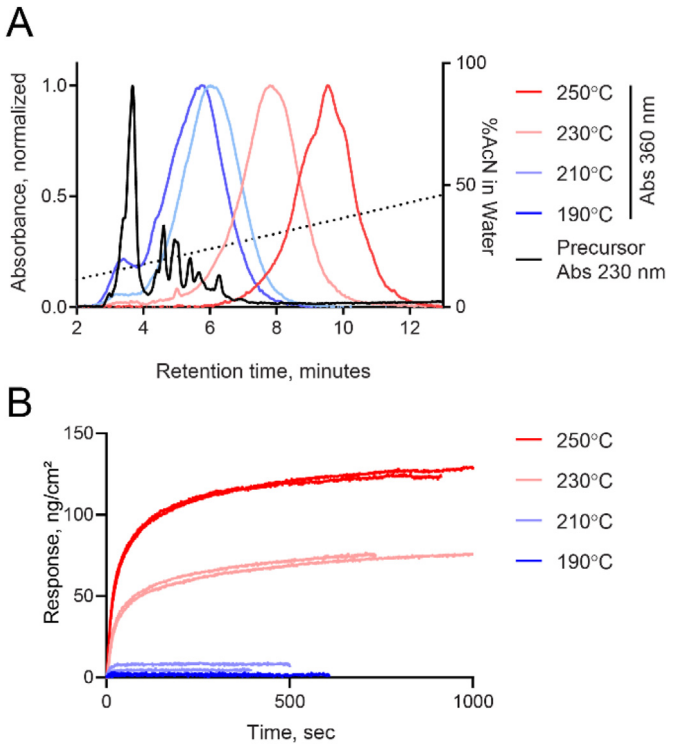

Fig. 4. Analysis of FCNs surface interactions by retention adsorption. **A.** Analytical high-performance liquid chromatography (HPLC) demonstrates retention and adsorption of FCNs using a C18 column from different pyrolysis conditions (250 μg injection, 1 mL/min, 3.17% AcN/min gradient with 0.1% TFA). Increased retention time indicates an increase in the relative hydrophobicity. The 360 nm absorbance is reported for the FCNs and the 230 nm absorbance is reported for the precursor, as shown in Fig. 3A. Fluorescence for the FCN runs was not available. **B.** Quartz crystal microbalance with dissipation monitoring (QCM-D) measurements of the adsorption of 0.05 mg/mL FCNs using a silica (SiO_2) sensor chip under flow (100 μL/min in 50 mM $CaCl_2$). (A colour version of this figure can be viewed online.)

In addition to examining the surface hydrophobicity, the adsorption of the FCNs to mineral surfaces was measured directly using a quartz crystal microbalance with dissipation monitoring (QCM-D) (Fig. 4B). Material adsorbed onto the resonator surface decreases the resonance frequency of the chip, allowing for sensitive measurement of adsorption mass per unit area [75]. The FCNs pyrolyzed at 190 and 210 °C showed little to no adsorption, while the FCN pyrolyzed at higher temperatures (230 and 250 °C) showed significant adsorption over baseline. Additional experiments probed the adsorption and desorption as a function of sample concentration using the FCNs prepared with 230 °C pyrolysis (Fig. S13). These experiments demonstrate a nonlinear adsorption with very little desorption. Silica and the slightly negatively charged FCNs are generally considered to be hydrophilic [26]. The adsorption agrees with the extended retention of the FCNs seen with HPLC in Fig. 4A. Together, these data suggest that a pyrolysis temperatures ≥230 °C increased the hydrophobicity of the FCNs and promoted their adsorption. As the pyrolysis proceeds at higher temperature, the carbonization could also be removing hydrophilic groups that would otherwise promote surface hydration of the FCNs, including those functional groups responsible for fluorescence. A relationship between fluorescence and hydrophilicity was also suggested by comparison of FCNs synthesized with malic and citric acid [27].

QCM-D experiments were conducted with the addition of both mono- and divalent salt (Fig. S14), which can influence nanoparticle adsorption if the adsorption is electrostatic in nature [26,43]. No significant difference was observed upon the addition of either mono- or divalent salt. This result indicates that the adsorption is not mediated by charge attraction, which could be screened by monovalent salt or promoted by divalent salts. Thus, this result is also in agreement that the adsorption is mediated by hydrophobicity of the FCNs.

Finally, the adsorption of the FCNs to the hydrophilic silica (SiO_2) QCM-D sensor chip suggests that other mineral surfaces could experience FCN adsorption. Thus, Fe_2O_3 and AlSiO coated QCM-D sensor chips were examined for FCN adsorption. These chips are

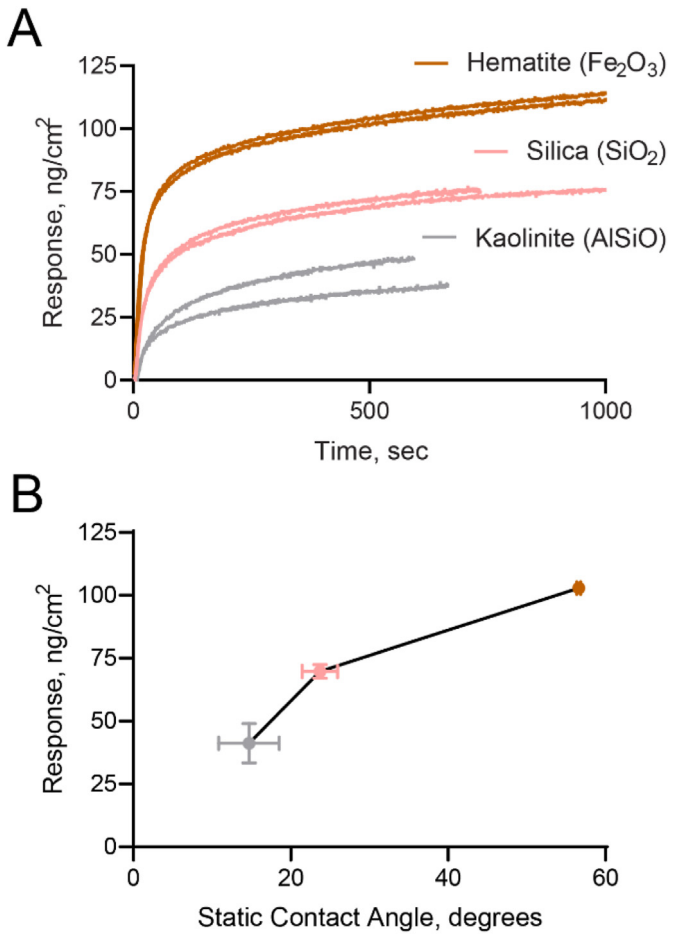

Fig. 5. A. Adsorption of FCNs onto mineral surfaces as observed by quartz crystal microbalance with dissipation monitoring (QCM-D) with silica (SiO_2 as in Fig. 4B), hematite (Fe_2O_3), and kaolinite (AlSiO) sensor chips. Measurements were performed under 100 μL/min in 50 mM $CaCl_2$ with 0.05 mg/mL 230 °C FCNs. **B.** Response of FCNs adsorption at 500 s versus the static contact angle measurements of the QCM-D sensor chips. Error is shown as the standard deviation of measurement for both the QCM-D response ($n = 2$, from Fig. 5A) and static contact angle measurement ($n = 3$). (A colour version of this figure can be viewed online.)

analogues for hematite (iron oxide) and kaolinite, respectively (Fig. 5A). The adsorption increased with the oxygen content of the chip (Fe_2O_3 > SiO_2 > AlSiO). Static contact angle measurements taken (water-air-surface) on the QCM-D sensor chips shows the hydrophobicity of the surfaces increases with the FCN adsorption ($Fe_2O_3 - 56.6 \pm 0.25°$ > $SiO_2 - 23.7 \pm 2.25°$ > $AlSiO - 14.7 \pm 3.85°$). FCN adsorption was greater for mineral surfaces that were more hydrophobic, indicating again that hydrophobicity is the mechanism of particle adsorption.

4. Conclusions

Our results have provided detail on the optimization of fluorescent carbon nanoparticles (FCNs) produced from citric acid and ethanolamine. Specifically, we controlled the synthesis conditions of pyrolysis to optimize their fluorescence and surface properties, both of which are paramount for their use as subsurface tracers and many other applications. Spectroscopic measurements were used to analyze the effect of pyrolysis conditions on fluorescence, and particle hydrophobicity was measured via HPLC. QCM-D was used to further probe particle hydrophobicity, and demonstrate adsorption to various mineral surfaces via hydrophobic interactions.

Our results support the generally reported mechanism of formation: molecular units polymerize and agglomerate during pyrolysis, likely through imide formation and subsequent condensation reactions [6,16,67]. Spectroscopic measurements, HPLC, and QCM-D together suggest that during the pyrolysis at modest temperatures (190–210 °C), hydrophilic and fluorescent functional groups form. Under these synthesis conditions, particles are highly fluorescent and hydrophilic, and show minimal absorption to mineral surfaces (<10 ng/cm^2). However, these hydrophilic functional groups are susceptible to further reaction and FCN carbonization as the pyrolysis temperature is elevated. This results in a loss of fluorescence and increased adsorption to mineral surfaces; this is detrimental for subsurface tracers. This adsorption to mineral surfaces was found to be insensitive to mono- and divalent ions, which has important implications for their intended application as subsurface nanoparticle tracers. Therefore, 210 °C was ideal to produce the most fluorescent FCNs that also minimally adsorb to mineral surfaces.

Further work is needed explore methods for tuning FCN size. To measure the stagnant porosity in natural systems, we need inert nanoparticles of greater size. Thirteen nanometer particles have a low diffusion constant, but still diffuse significantly into stagnant areas for long distance tests in warm reservoirs where tracer transit takes years. Additionally, further work will explore the aggregation behavior and stability of these FCNs as affected by their pyrolysis, as increased surface hydrophobicity could drive aggregation. Additionally, tracer tests in flow-through columns containing sand or other geological samples can be used to scale up the observations of this study. Column tests can be useful for quantifying adsorption onto heterogeneous mineral surfaces and further probing the effect of dissolved solids. If similar mineral compositions are utilized in the column tests, modeling and extrapolation of the QCM-D results can be pursued. Tracer tests in columns will be important in eventual interpretation of field tracer tests.

The ability to easily tune nanoparticle surface properties has wide applications, including subsurface nanoparticle tracers examined herein. With the ubiquitous consideration of nanoparticle surface hydrophobicity affecting the biological application of nanoparticles [54,56], this work also has implications for other formulations of fluorescent carbon nanoparticles for applications in biological sensing, imaging, and more.

CRediT authorship contribution statement

Laura Sinclair: Methodology, Investigation, Writing - original draft, Visualization. **Joseph Brown:** Methodology, Formal analysis, Investigation, Writing - original draft, Visualization. **Muhammad G. Salim:** Investigation, Methodology, Visualization, Writing - review & editing. **Daniel May:** Conceptualization, Methodology, Writing - review & editing. **Bahareh Guilvaiee:** Conceptualization, Methodology, Writing - review & editing. **Adam Hawkins:** Conceptualization, Writing - review & editing. **Lawrence Cathles:** Conceptualization, Methodology, Writing - review & editing, Supervision, Funding acquisition.

Declaration of competing interest

The authors declare that they have no known competing financial interests or personal relationships that could have appeared to influence the work reported in this paper.

Acknowledgements

The authors acknowledge Professor Chris Alabi (Chemical Engineering, Cornell University) for analytical equipment support

with Cornell University Startup funds and the Nancy and Peter Meinig Investigator Fellowship. J.S.B acknowledges financial support from the National Science Foundation Graduate Research Fellowship Program (DGE-1650441). L.K.S and L.M.C. gratefully acknowledge the support of the Pall Corporation, the Norwegian Increased Oil Recovery Project, and Florence Copper. This work made use of the Cornell University NMR Facility, which is supported in part by the NSF through MRI award CHE-1531632, and the Cornell Center for Materials Research Shared Facilities which are supported through the NSF MRSEC program (DMR-1719875).

Appendix A. Supplementary data

Supplementary data to this article can be found online at https://doi.org/10.1016/j.carbon.2020.07.024.

References

[1] Q. Xu, W. Li, L. Ding, W. Yang, H. Xiao, W.J. Ong, Function-driven engineering of 1D carbon nanotubes and 0D carbon dots: mechanism, properties and applications, Nanoscale 11 (4) (2019) 1475–1504, https://doi.org/10.1039/c8nr08738e.
[2] S.N. Baker, G.A. Baker, Luminescent carbon nanodots: emergent nanolights, Angew. Chem. Int. Ed. 49 (38) (2010) 6726–6744, https://doi.org/10.1002/anie.200906623.
[3] Y. Wang, A. Hu, Carbon quantum dots: synthesis, properties and applications, J. Mater. Chem. C 2 (34) (2014) 6921, https://doi.org/10.1039/C4TC00988F.
[4] J.B. Essner, J.A. Kist, L. Polo-Parada, G.A. Baker, Artifacts and errors associated with the ubiquitous presence of fluorescent impurities in carbon nanodots, Chem. Mater. 30 (6) (2018) 1878–1887, https://doi.org/10.1021/acs.chemmater.7b04446.
[5] D. Qu, Z. Sun, The formation mechanism and fluorophores of carbon dots synthesized: via a bottom-up route, Mater. Chem. Front. 4 (2) (2020) 400–420, https://doi.org/10.1039/c9qm00552h.
[6] S. Zhu, Y. Song, X. Zhao, J. Shao, J. Zhang, B. Yang, The photoluminescence mechanism in carbon dots (graphene quantum dots, carbon nanodots, and polymer dots): current state and future perspective, Nano Res 8 (2) (2015) 355–381, https://doi.org/10.1007/s12274-014-0644-3.
[7] H. Ding, S.B. Yu, J.S. Wei, H.M. Xiong, Full-color light-emitting carbon dots with a surface-state-controlled luminescence mechanism, ACS Nano 10 (1) (2016) 484–491, https://doi.org/10.1021/acsnano.5b05406.
[8] L. Cao, X. Wang, M.J. Meziani, F. Lu, H. Wang, P.G. Luo, Y. Lin, B.A. Harruff, L.M. Veca, D. Murray, et al., Carbon dots for multiphoton bioimaging, J. Am. Chem. Soc. 129 (37) (2007) 11318–11319, https://doi.org/10.1021/ja073527l.
[9] H. Liu, T. Ye, C. Mao, Fluorescent carbon nanoparticles derived from candle soot, Angew. Chem. Int. Ed. 46 (34) (2007) 6473–6475, https://doi.org/10.1002/anie.200701271.
[10] S.C. Ray, A. Saha, N.R. Jana, R. Sarkar, Fluorescent carbon nanoparticles: synthesis, characterization, and bioimaging application, J. Phys. Chem. C 113 (43) (2009) 18546–18551, https://doi.org/10.1021/jp905912n.
[11] H. Li, X. He, Z. Kang, H. Huang, Y. Liu, J. Liu, S. Lian, C.H.A. Tsang, X. Yang, S.T. Lee, Water-soluble fluorescent carbon quantum dots and photocatalyst design, Angew. Chem. Int. Ed. 49 (26) (2010) 4430–4434, https://doi.org/10.1002/anie.200906154.
[12] L. Bao, Z.L. Zhang, Z.Q. Tian, L. Zhang, C. Liu, Y. Lin, B. Qi, D.W. Pang, Electrochemical tuning of luminescent carbon nanodots: from preparation to luminescence mechanism, Adv. Mater. 23 (48) (2011) 5801–5806, https://doi.org/10.1002/adma.201102866.
[13] J. Peng, W. Gao, B.K. Gupta, Z. Liu, R. Romero-Aburto, L. Ge, L. Song, L.B. Alemany, X. Zhan, G. Gao, et al., Graphene quantum dots derived from carbon fibers, Nano Lett. 12 (2) (2012) 844–849, https://doi.org/10.1021/nl2038979.
[14] S.C. Hens, W.G. Lawrence, A.S. Kumbhar, O. Shenderova, Photoluminescent nanostructures from graphite oxidation, J. Phys. Chem. C 116 (37) (2012) 20015–20022, https://doi.org/10.1021/jp303061e.
[15] S. Zhuo, M. Shao, S.T. Lee, Upconversion and downconversion fluorescent graphene quantum dots: ultrasonic preparation and photocatalysis, ACS Nano 6 (2) (2012) 1059–1064, https://doi.org/10.1021/nn2040395.
[16] M.J. Krysmann, A. Kelarakis, P. Dallas, E.P. Giannelis, Formation mechanism of carbogenic nanoparticles with dual photoluminescence emission, J. Am. Chem. Soc. 134 (2) (2012) 747–750, https://doi.org/10.1021/ja204661r.
[17] Y. Fang, S. Guo, D. Li, C. Zhu, W. Ren, S. Dong, E. Wang, Easy synthesis and imaging applications of cross-linked green fluorescent hollow carbon nanoparticles, ACS Nano 6 (1) (2012) 400–409, https://doi.org/10.1021/nn2046373.
[18] Y. Dong, H. Pang, H. Bin Yang, C. Guo, J. Shao, Y. Chi, C.M. Li, T. Yu, Carbon-based dots Co-doped with nitrogen and sulfur for high quantum yield and excitation-independent emission, Angew. Chem. Int. Ed. 52 (30) (2013) 7800–7804, https://doi.org/10.1002/anie.201301114.
[19] Q. Fang, Y. Dong, Y. Chen, C.H. Lu, Y. Chi, H.H. Yang, T. Yu, Luminescence origin of carbon based dots obtained from citric acid and amino group-containing molecules, Carbon N. Y. 118 (2017) 319–326, https://doi.org/10.1016/j.carbon.2017.03.061.
[20] R. Liu, D. Wu, S. Liu, K. Koynov, W. Knoll, Q. Li, An aqueous route to multicolor photoluminescent carbon dots using silica spheres as carriers, Angew. Chem. Int. Ed. 48 (25) (2009) 4598–4601, https://doi.org/10.1002/anie.200900652.
[21] H. Li, X. He, Y. Liu, H. Huang, S. Lian, S.T. Lee, Z. Kang, One-step ultrasonic synthesis of water-soluble carbon nanoparticles with excellent photoluminescent properties, Carbon N. Y. 49 (2) (2011) 605–609, https://doi.org/10.1016/j.carbon.2010.10.004.
[22] S. Chandra, S.H. Pathan, S. Mitra, B.H. Modha, A. Goswami, P. Pramanik, Tuning of photoluminescence on different surface functionalized carbon quantum dots, RSC Adv. 2 (9) (2012) 3602–3606, https://doi.org/10.1039/c2ra00030j.
[23] L. Shi, J.H. Yang, H.B. Zeng, Y.M. Chen, S.C. Yang, C. Wu, H. Zeng, O. Yoshihito, Q. Zhang, Carbon dots with high fluorescence quantum yield: the fluorescence originates from organic fluorophores, Nanoscale 8 (30) (2016) 14374–14378, https://doi.org/10.1039/c6nr00451b.
[24] J. Schneider, C.J. Reckmeier, Y. Xiong, M. Von Seckendorff, A.S. Susha, P. Kasak, A.L. Rogach, Molecular fluorescence in citric acid-based carbon dots, J. Phys. Chem. C 121 (3) (2017) 2014–2022, https://doi.org/10.1021/acs.jpcc.6b12519.
[25] S. Bhattacharyya, F. Ehrat, P. Urban, R. Teves, R. Wyrwich, M. Döblinger, J. Feldmann, A.S. Urban, J.K. Stolarczyk, Effect of nitrogen atom positioning on the trade-off between emissive and photocatalytic properties of carbon dots, Nat. Commun. 8 (1) (2017) 1–9, https://doi.org/10.1038/s41467-017-01463-x.
[26] Y.V. Li, L.M. Cathles, L.A. Archer, Nanoparticle tracers in calcium carbonate porous media, J. Nanoparticle Res. 16 (8) (2014), https://doi.org/10.1007/s11051-014-2541-9.
[27] Y.V. Li, L.M. Cathles, The surface interactions of a near-neutral carbon nanoparticle tracer with calcite, J. Nanoparticle Res. 18 (3) (2016) 1–14, https://doi.org/10.1007/s11051-016-3383-4.
[28] D. Kosynkin, M. Alaskar, Oil industry first interwell trial of reservoir nanoagent tracers, in: SPE Annual Technical Conference and Exhibition, Society of Petroleum Engineers, Dubai, UAE, 2016, p. 15, https://doi.org/10.2118/181551-MS.
[29] E.S. Ellis, M.N. Askar, M. Hotan, H. Shateeb, Successful field test of real time inline sensing system for tracer detection at well head, Soc. Pet. Eng. - SPE Kingdom Saudi Arab. Annu. Tech. Symp. Exhib. (2017) 2049–2066, 2017.
[30] B. Berkowitz, Characterizing flow and transport in fractured geological media: a review, Adv. Water Resour. 25 (2002) 861–884, https://doi.org/10.1016/S0309-1708(02)00042-8.
[31] M.W. Becker, A.M. Shapiro, Tracer transport in fractured crystalline rock: evidence of nondiffusive breakthrough tailing, Water Resour. Res. 36 (7) (2000) 1677, https://doi.org/10.1029/2000WR900080.
[32] A.J. Hawkins, M.W. Becker, G.P. Tsoflias, Evaluation of inert tracers in a bedrock fracture using ground penetrating radar and thermal sensors, Geothermics 67 (2017) 86–94, https://doi.org/10.1016/j.geothermics.2017.01.006.
[33] L.K. Sinclair, J.F.H. Thompson, In situ leaching of copper: challenges and future prospects, Hydrometallurgy 157 (2015) 306–324, https://doi.org/10.1016/j.hydromet.2015.08.022.
[34] G.E. Grisak, J.F. Pickens, J.A. Cherry, Solute transport through fractured media: 2. Column study of fractured till, Water Resour. Res. 16 (4) (1980) 731–739, https://doi.org/10.1029/WR016i004p00731.
[35] L.D. McKay, R.W. Gillham, J.A. Cherry, Field experiments in a fractured clay till: 2. Solute and colloid transport, Water Resour. Res. 29 (12) (1993) 3879–3890, https://doi.org/10.1029/93WR02069.
[36] L.M. Cathles, H.R. Spedden, E.E. Malouf, A tracer technique to measure the diffusional accessibility of matrix block mineralization, in: F.F. Aplan, W.A. McKinney, A.D. Pernichele (Eds.), Solution Mining Symposium, American Institute of Mining, Metallurgical, and Petroleum Engineers, New York, NY, 1974, pp. 129–147.
[37] S.K. Subramanian, Y. Li, L.M. Cathles, Assessing preferential flow by simultaneously injecting nanoparticle and chemical tracers, Water Resour. Res. 49 (2013) 29–42, https://doi.org/10.1029/2012WR012148.
[38] A.J. Hawkins, M.W. Becker, J.W. Tester, Inert and adsorptive tracer tests for field measurement of flow-wetted surface area, Water Resour. Res. 54 (8) (2018) 5341–5358, https://doi.org/10.1029/2017WR021910.
[39] A.J. Hawkins, D.B. Fox, M.W. Becker, J.W. Tester, Measurement and simulation of heat exchange in fractured bedrock using inert and thermally degrading tracers, Water Resour. Res. 53 (2) (2017) 1210–1230, https://doi.org/10.1002/2016WR019617.
[40] C. Serres-Piole, H. Preud'homme, N. Moradi-Tehrani, C. Allanic, H. Jullia, R. Lobinski, Water tracers in oilfield applications: guidelines, J. Petrol. Sci. Eng. 98–99 (2012) 22–39, https://doi.org/10.1016/j.petrol.2012.08.009.
[41] A. Hawkins, L.M. Cathles, R. Zhao, Comparison of C-dot nanoparticle and iodide breakthrough curves in a shallow fracture-dominated aquifer, in: Geological Society of America'a Annual Meeting, 2015. Baltimore, MD.
[42] S. Li, O. Torsæter, H.C. Lau, N.J. Hadia, L.P. Stubbs, The impact of nanoparticle adsorption on transport and wettability alteration in water-wet berea sandstone: an experimental study, Front. Physiol. 7 (May) (2019) 1–12, https://doi.org/10.3389/fphy.2019.00074.
[43] S. Simovic, C.A. Prestidge, Adsorption of hydrophobic silica nanoparticles at the PDMS droplet-water interface, Langmuir 19 (20) (2003) 8364–8370, https://doi.org/10.1021/la0347197.

[44] F. Meierhofer, F. Dissinger, F. Weigert, J. Jungclaus, K. Müller-Caspary, S.R. Waldvogel, U. Resch-Genger, T. Voss, Citric acid based carbon dots with amine type stabilizers: PH-specific luminescence and quantum yield characteristics, J. Phys. Chem. C 124 (16) (2020) 8894–8904, https://doi.org/10.1021/acs.jpcc.9b11732.
[45] E. Rodriguez, M.R. Roberts, H. Yu, C. Huh, S.L. Bryant, Enhanced migration of surface-treated nanoparticles in sedimentary rocks, Proc. - SPE Annu. Tech. Conf. Exhib. 4 (2009) 2058–2078.
[46] H. Yu, C. Kotsmar, K.Y. Yoon, D.R. Ingram, K.P. Johnston, S.L. Bryant, C. Huh, Transport and retention of aqueous dispersions of paramagnetic nanoparticles in reservoir rocks, Proc. - SPE Symp. Improv. Oil Recover. 2 (2010) 1027–1047.
[47] I.G. Godinez, C.J.G. Darnault, Aggregation and transport of nano-TiO2 in saturated porous media: effects of PH, surfactants and flow velocity, Water Res. 45 (2) (2011) 839–851, https://doi.org/10.1016/j.watres.2010.09.013.
[48] J. Brant, H. Lecoanet, M.R. Wiesner, Aggregation and deposition characteristics of fullerene nanoparticles in aqueous systems, J. Nanoparticle Res. 7 (4–5) (2005) 545–553, https://doi.org/10.1007/s11051-005-4884-8.
[49] M. Alaskar, M. Ames, S. Connor, C. Liu, Y. Cui, K. Li, R. Home, Nanoparticle and microparticle flow in porous and fractured media- an experimental study, SPE J. 17 (4) (2012) 1160–1171.
[50] R.A. Petros, J.M. DeSimone, Strategies in the design of nanoparticles for therapeutic applications, Nat. Rev. Drug Discov. 9 (8) (2010) 615–627, https://doi.org/10.1038/nrd2591.
[51] A. Verma, F. Stellacci, Effect of surface properties on nanoparticle-cell interactions, Small 6 (1) (2010) 12–21, https://doi.org/10.1002/smll.200901158.
[52] G. Azimi, R. Dhiman, H. Kwon, A.T. Paxson, K.K. Varanasi, Hydrophobicity of rare-earth oxide ceramics, Nat. Mater. 12 (4) (2013) 315–320, https://doi.org/10.1038/nmat3545.
[53] S. Khan, G. Azimi, B. Yildiz, K.K. Varanasi, Role of surface oxygen-to-metal ratio on the wettability of rare-earth oxides, Appl. Phys. Lett. 106 (6) (2015) 2–7, https://doi.org/10.1063/1.4907756.
[54] M. Lundqvist, J. Stigler, G. Elia, I. Lynch, T. Cedervall, K.A. Dawson, Nanoparticle size and surface properties determine the protein corona with possible implications for biological impacts, Proc. Natl. Acad. Sci. U.S.A. 105 (38) (2008) 14265–14270, https://doi.org/10.1073/pnas.0805135105.
[55] P. Aggarwal, J.B. Hall, C.B. McLeland, M.A. Dobrovolskaia, S.E. McNeil, Nanoparticle interaction with plasma proteins as it relates to particle biodistribution, biocompatibility and therapeutic efficacy, Adv. Drug Deliv. Rev. 61 (6) (2009) 428–437, https://doi.org/10.1016/j.addr.2009.03.009.
[56] M.P. Monopoli, C. Åberg, A. Salvati, K.A. Dawson, Biomolecular coronas provide the biological identity of nanosized materials, Nat. Nanotechnol. 7 (12) (2012) 779–786, https://doi.org/10.1038/nnano.2012.207.
[57] F. Shima, T. Akagi, T. Uto, M. Akashi, Manipulating the antigen-specific immune response by the hydrophobicity of amphiphilic poly(γ-glutamic acid) nanoparticles, Biomaterials 34 (37) (2013) 9709–9716, https://doi.org/10.1016/J.BIOMATERIALS.2013.08.064.
[58] D.F. Moyano, M. Goldsmith, D.J. Solfiell, D. Landesman-Milo, O.R. Miranda, D. Peer, V.M. Rotello, Nanoparticle hydrophobicity dictates immune response, J. Am. Chem. Soc. 134 (9) (2012) 3965–3967, https://doi.org/10.1021/ja2108905.
[59] D.F. Moyano, K. Saha, G. Prakash, B. Yan, H. Kong, M. Yazdani, V.M. Rotello, Fabrication of corona-free nanoparticles with tunable hydrophobicity, ACS Nano 8 (7) (2014) 6748–6755, https://doi.org/10.1021/nn5006478.
[60] Y. Xiao, M.R. Wiesner, Characterization of surface hydrophobicity of engineered nanoparticles, J. Hazard Mater. 215–216 (2012) 146–151, https://doi.org/10.1016/j.jhazmat.2012.02.043.
[61] C. Desmet, A. Valsesia, A. Oddo, G. Ceccone, V. Spampinato, F. Rossi, P. Colpo, Characterisation of nanomaterial hydrophobicity using engineered surfaces, J. Nanoparticle Res. 19 (3) (2017), https://doi.org/10.1007/s11051-017-3804-z.
[62] A. Valsesia, C. Desmet, I. Ojea-Jiménez, A. Oddo, R. Capomaccio, F. Rossi, P. Colpo, Direct quantification of nanoparticle surface hydrophobicity, Commun. Chem. 1 (1) (2018) 53, https://doi.org/10.1038/s42004-018-0054-7.
[63] V.K. Gupta, T.A. Saleh, Sorption of pollutants by porous carbon, carbon nanotubes and fullerene- an overview, Environ. Sci. Pollut. Res. 20 (5) (2013) 2828–2843, https://doi.org/10.1007/s11356-013-1524-1.
[64] Z. Bagheri, H. Ehtesabi, M. Rahmandoust, M.M. Ahadian, Z. Hallaji, F. Eskandari, E. Jokar, New insight into the concept of carbonization degree in synthesis of carbon dots to achieve facile smartphone based sensing platform, Sci. Rep. 7 (1) (2017) 1–11, https://doi.org/10.1038/s41598-017-11572-8.
[65] X. Liu, H.B. Li, L. Shi, X. Meng, Y. Wang, X. Chen, H. Xu, W. Zhang, X. Fang, T. Ding, Structure and photoluminescence evolution of nanodots during pyrolysis of citric acid: from molecular nanoclusters to carbogenic nanoparticles, J. Mater. Chem. C 5 (39) (2017) 10302–10312, https://doi.org/10.1039/c7tc03429f.
[66] G. Sauerbrey, Verwendung von Schwingquarzen zur wägung dünner schichten und zur mikrowägung, Zeitschrift für Phys. 155 (2) (1959) 206–222, https://doi.org/10.1007/BF01337937.
[67] Y. Song, S. Zhu, S. Zhang, Y. Fu, L. Wang, X. Zhao, B. Yang, Investigation from chemical structure to photoluminescent mechanism: a type of carbon dots from the pyrolysis of citric acid and an amine, J. Mater. Chem. C 3 (23) (2015) 5976–5984, https://doi.org/10.1039/c5tc00813a.
[68] N. Dhenadhayalan, K.C. Lin, R. Suresh, P. Ramamurthy, Unravelling the multiple emissive states in citric-acid-derived carbon dots, J. Phys. Chem. C 120 (2) (2016) 1252–1261, https://doi.org/10.1021/acs.jpcc.5b08516.
[69] S. Zhu, J. Zhang, S. Tang, C. Qiao, L. Wang, H. Wang, X. Liu, B. Li, Y. Li, W. Yu, et al., Surface chemistry routes to modulate the photoluminescence of graphene quantum dots: from fluorescence mechanism to up-conversion bioimaging applications, Adv. Funct. Mater. 22 (22) (2012) 4732–4740, https://doi.org/10.1002/adfm.201201499.
[70] A. Gruber, A. Dräbenstedt, C. Tietz, L. Fleury, J. Wrachtrup, C. Von Borczyskowski, Scanning confocal optical microscopy and magnetic resonance on single defect centers, Science (80) 276 (5321) (1997) 2012–2014, https://doi.org/10.1126/science.276.5321.2012.
[71] Q. Wang, B. Xu, Q. Hao, D. Wang, H. Liu, L. Jiang, In situ reversible underwater superwetting transition by electrochemical atomic alternation, Nat. Commun. 10 (1) (2019), https://doi.org/10.1038/s41467-019-09201-1.
[72] X. Gong, M. Chin Paau, Q. Hu, S. Shuang, C. Dong, M.M.F. Choi, UHPLC combined with mass spectrometric study of as-synthesized carbon dots samples, Talanta 146 (2016) 340–350, https://doi.org/10.1016/j.talanta.2015.08.051.
[73] Q. Hu, M.C. Paau, M.M.F. Choi, Y. Zhang, X. Gong, L. Zhang, Y. Liu, J. Yao, Better understanding of carbon nanoparticles via high-performance liquid chromatography-fluorescence detection and mass spectrometry, Electrophoresis 35 (17) (2014) 2454–2462, https://doi.org/10.1002/elps.201400197.
[74] J.C. Vinci, I.M. Ferrer, S.J. Seedhouse, A.K. Bourdon, J.M. Reynard, B.A. Foster, F.V. Bright, L.A. Colón, Hidden properties of carbon dots revealed after HPLC fractionation, J. Phys. Chem. Lett. 4 (2) (2013) 239–243, https://doi.org/10.1021/jz301911y.
[75] Q. Chen, S. Xu, Q. Liu, J. Masliyah, Z. Xu, QCM-D study of nanoparticle interactions, Adv. Colloid Interface Sci. 233 (2016) 94–114, https://doi.org/10.1016/j.cis.2015.10.004.

Optimization of fluorescence and surface adsorption of citric acid/ethanolamine carbon nanoparticles for subsurface tracers

Laura Sinclair[1‡]*, Joseph Brown[1,2‡], Muhammad G. Salim[3], Daniel May[4], Bahareh Guilvaiee[5], Adam Hawkins[4], and Lawrence Cathles[4]

[1] Robert F. Smith School of Chemical and Biomolecular Engineering, Cornell University, Ithaca, NY, USA
[2] Department of Chemistry, Massachusetts Institute of Technology, Cambridge, MA, USA
[3] Cornell Center for Materials Research, Cornell University, Ithaca, NY, USA
[4] Department of Earth and Atmospheric Sciences, Cornell University, Ithaca, NY, USA
[5] Department of Biological and Environmental Engineering, Cornell University, Ithaca, NY, USA
[‡]These authors contributed equally. *Corresponding Author: lks82@cornell.edu

Supporting Information

Table S1. Summary of critic acid/ethanolamine fluorescent carbon nanoparticle properties.

Property	Pyrolysis	Amount	Reference
Yield, by mass	190 ºC	2%	(this work)
	210 ºC	4%	(this work)
	230 ºC	7%	(this work)
	250 ºC	26%	(this work)
Size (diameter)	190 ºC	12.4 ± 5.6 nm by TEM, n=333	(this work)
	200 ºC	3.5 ± 2.1 nm by DLS	Y. Li et al. J Nanoparticle Res. (2014)[1]
	210 ºC	15.9 ± 11.7 nm by TEM, n=70	(this work)
	230 ºC	12.5 ± 7.0 nm by TEM, n=238	(this work)
	230 ºC	19 ± 2 nm by TEM, n=150	(M. J. Krysmann et al., JACS, 2012)[2]
	250 ºC	13.2 ± 7.4 nm by TEM, n=94	(this work)
	300 ºC	8 ± 2.5 nm by TEM, n=150	(M. J. Krysmann et al., JACS, 2012)[2]
Surface charge	200 ºC	-1.5 ± 2.0 mV by DLS in DI Water, pH 7.35	Y. Li et al. J Nanoparticle Res. (2014)[1]
	200 ºC	-0.88 ± 3.4 mV by DLS in 'Oil Field Brine' (2.21 M NaCl, 0.74 M $CaCl_2$, 0.18 M $MgCl_2$), pH 6.34	Y. Li, et al., J Nanoparticle Res. (2014)[1]
Quantum Yield	180 ºC	50%	(M. J. Krysmann et al., JACS, 2012)[2]
	190 ºC	11%	(this work)
	210 ºC	16%	(this work)
	230 ºC	15%	(M. J. Krysmann et al., JACS, 2012)[2]
	230 ºC	10%	(this work)
	250 ºC	4%	(this work)
	300 ºC	4%	(M. J. Krysmann et al., JACS, 2012)[2]

TEM: Transmission electron microscopy; DLS: dynamic light scattering; Quantum Yield of nanoparticle solutions (0.01 – 0.1 mg/mL) was quantified following D. F. Eaton., Pure & Appl. Chem. 60, (1988) pp. 1107 with reference to BODIPY FL (4,4-Difluoro-5,7-dimethyl-4-bora-3a,4a-

diaza-s-indacene-3-propionic acid, 3 ng/mL – 3 µg/mL) using a TECAN Infinite® M1000 PRO Microplate Reader (Männdorf, Switzerland) with Greiner UV-Star® flat bottom 96 well plates.

NMR

Nuclear Magnetic Resonance (NMR) spectra of the diamide/triamide product (purified from the precursor via HPLC as described in the Main Text) were recorded on a Varian Unity INOVA 600MHz with a Varian 600 triple resonance XYZ PFG (HCN) inverted probe or a Bruker INOVA 500MHz spectrometer with cryoprobe at the Cornell University NMR Facility. Spectra were analyzed by MestReNova (version 10.0.0). ^{1}H NMR chemical shifts are reported in units of ppm relative to deuterated solvent. The ^{13}C results point to the presence of the triamide product (see Figure S1 and Figure S2).

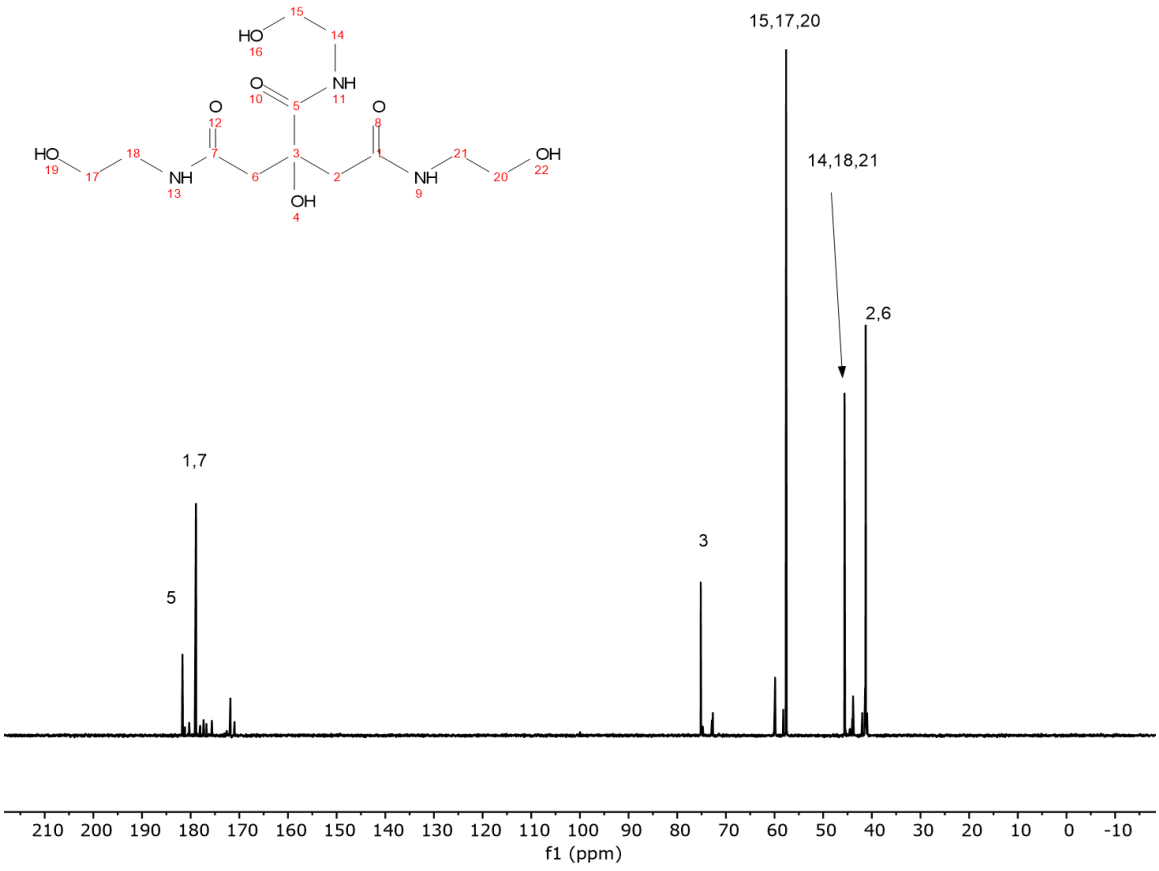

Figure S1 - ^{13}C NMR of diamide/triamide product purified from the precursor.

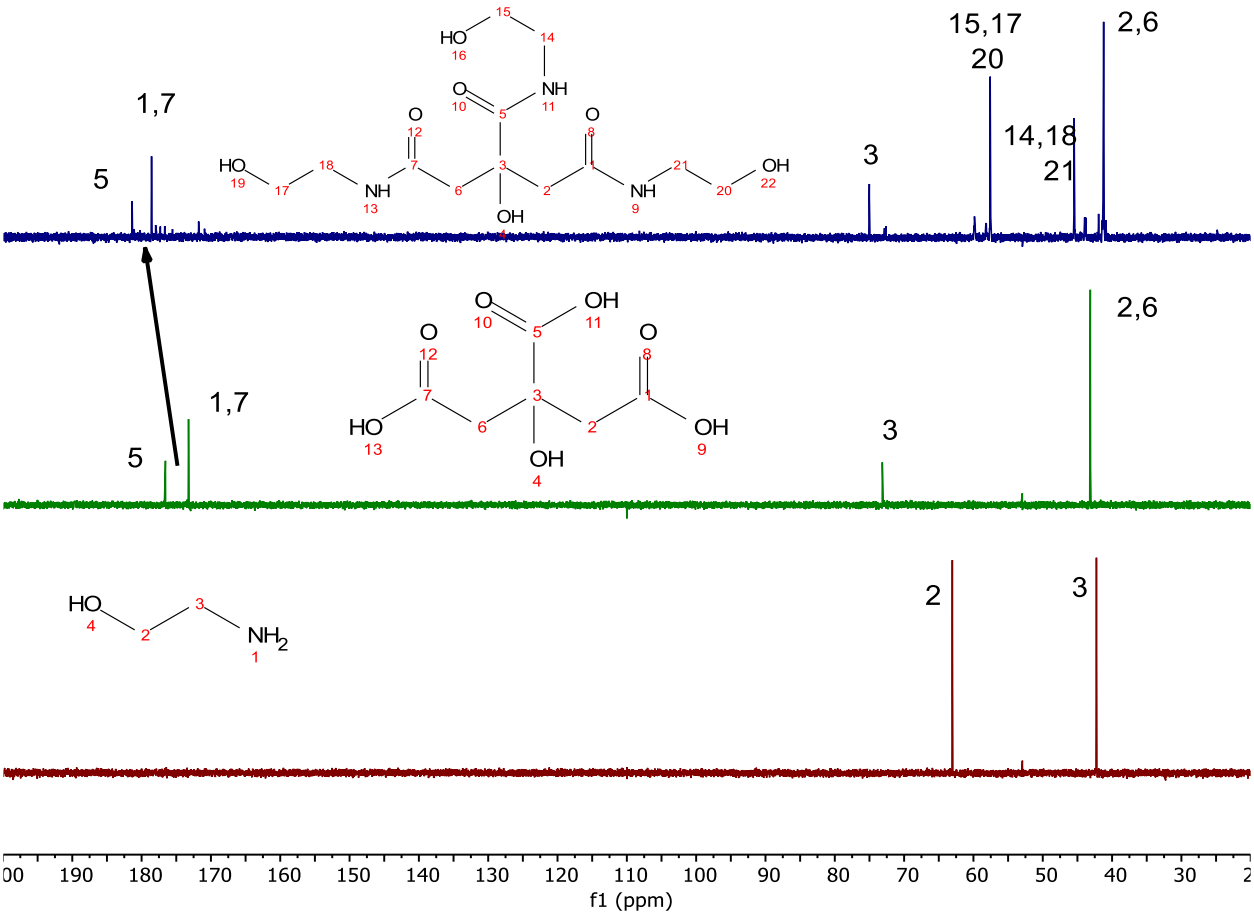

Figure S2 – ^{13}C NMR of diamide/triamide product purified from the precursor, along with citric acid and ethanolamine.

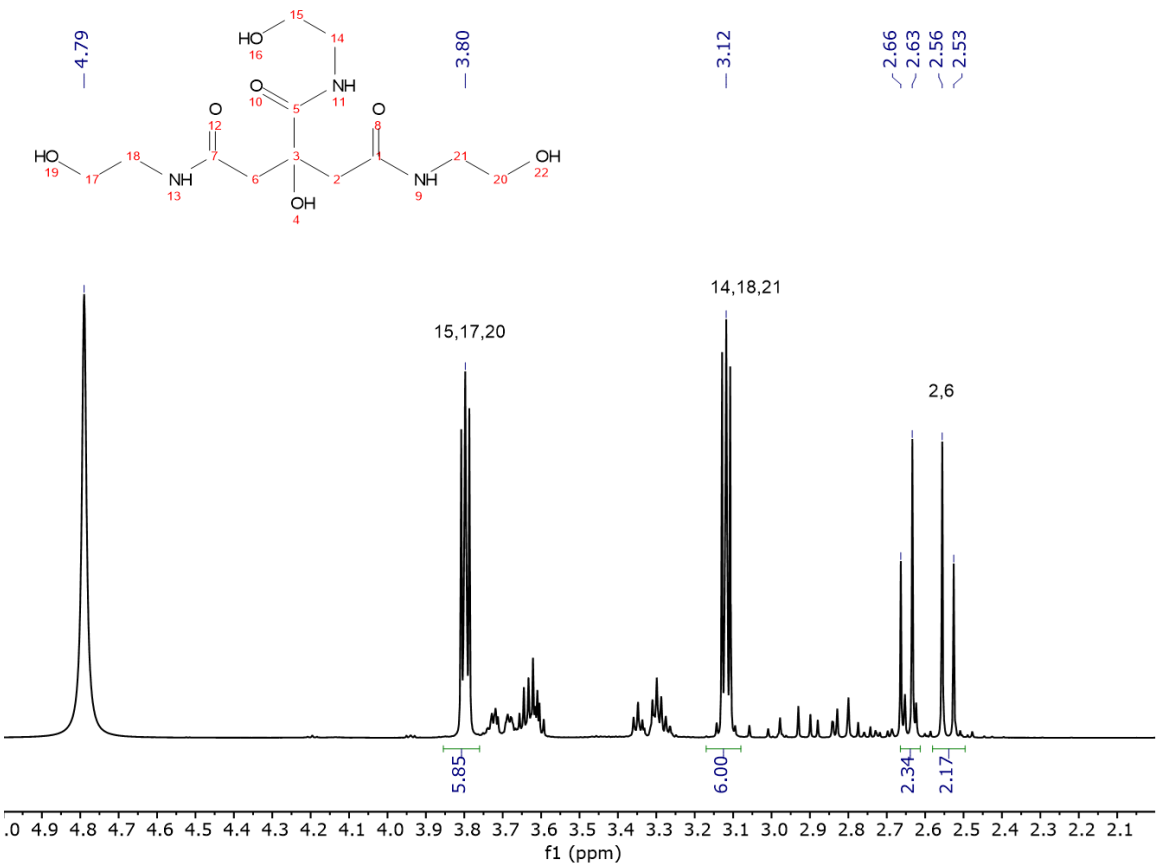

Figure S3 - ^{1}H NMR of diamide/triamide product purified from the precursor.

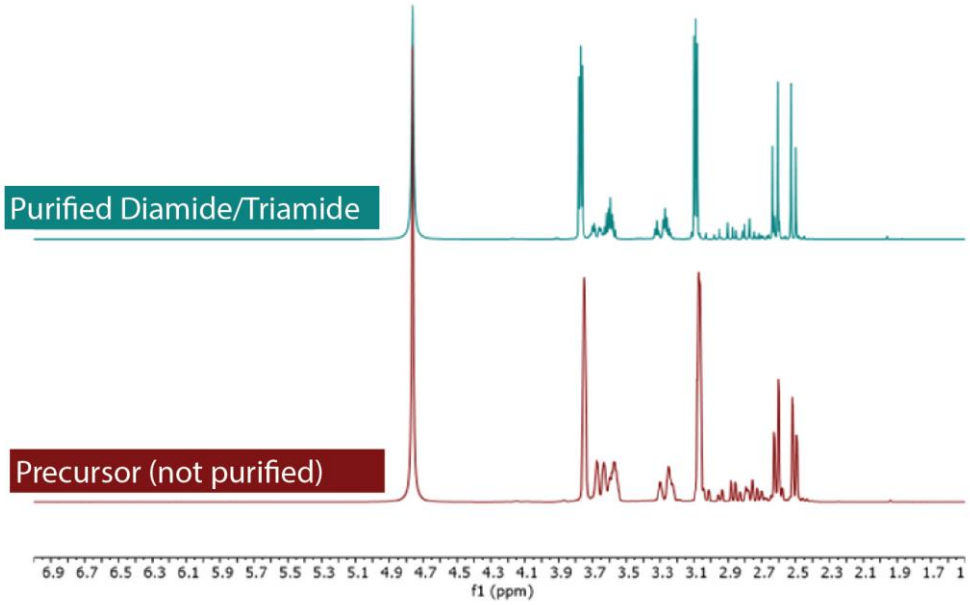

Figure S4 - ^{1}H NMR of diamide/triamide product purified from the precursor, and precursor (not purified)

LCMS

Liquid Chromatography Mass Spectrometry (LCMS) was performed on the precursor (not purified). LCMS experiments were carried out on an Agilent 1100 LCMS system with a Poroshell 120 EC-C18 (3.0x100mm, 2.7µm) column monitoring at 210 nm in positive mode for detection. Solvents for LCMS were water with 0.1% acetic acid (solvent A) and acetonitrile with 0.1% acetic acid (solvent B). A flow rate of 0.6 mL/min was used with a solvent B concentration starting at 5% and then increasing linearly with time from 5% to 100% solvent B over 10 min, remaining at 100% solvent B for 2 min, and then returning abruptly to 5% solvent B until equilibrated (3 min).

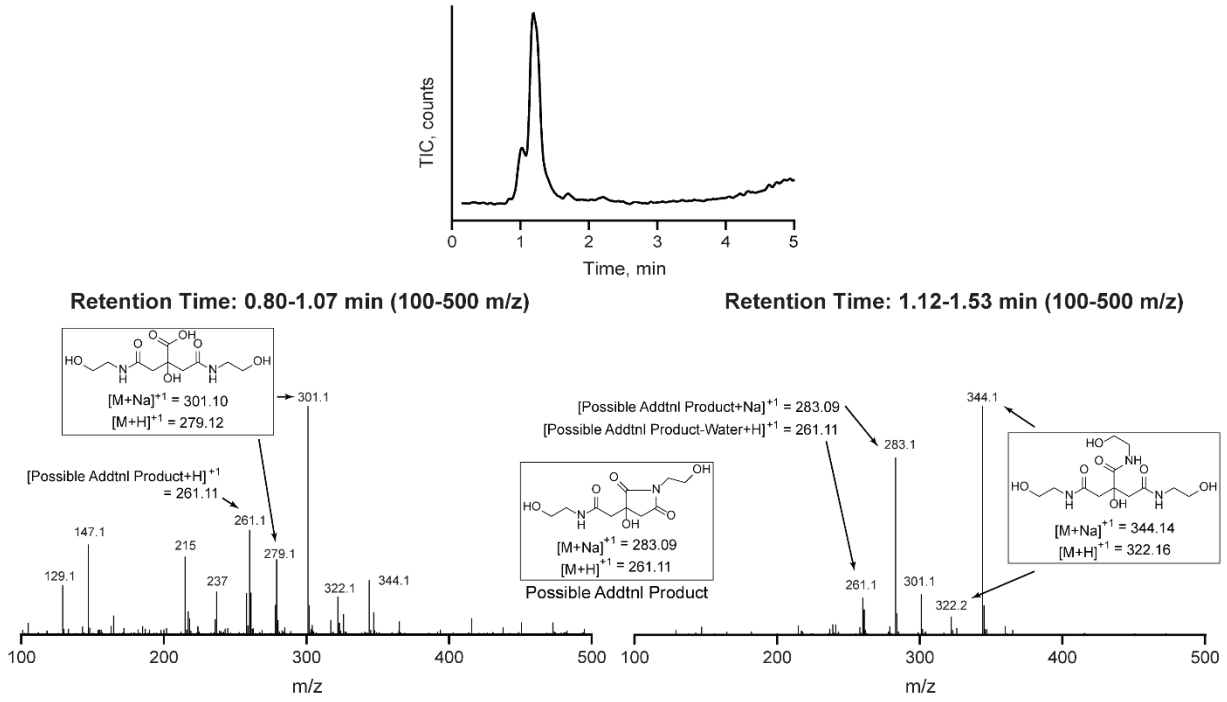

Figure S5 - LCMS results of precursor with the major peak observed mass spectra of the triamide product. The diamide product was also observed as a shoulder eluting before the triamide product. There was also evidence for a possible additional product highlighted in the center that could be formed from the additional condensation of the triamide product. This product is significant because it similarly matches the pathway of observed citrazinic acid derivatives in FCNs prepared from citric acid and ethylene diamine.[3–5]

Transmission Electron Microscopy

Transmission Electron Microscopy (FEI T12 Spirit, 120 kV field emission) was used to image particles after dialysis and freeze drying. The particles were suspended in water at 10 mg/mL and sonicated for 20 minutes. 5 µL was pipetted onto a grid and then blotted. Ultra-thin carbon grids were used in order to provide sufficient contrast in the images. Image J was used to obtain particle size distributions for each pyrolysis temperature as mentioned in the Main Text. At least 70 particles at each pyrolysis temperature were analyzed, using between three and five images. The particle size distributions were not statistically different from each other, all centered at approximately 13 nm diameter, with a significant right skew to the distribution (Figure 2 in Main Text). This is generally in agreement with a previous study which found the mean particle size to be 19 nm.[2] Full-sized images are shown below in Figure S6.

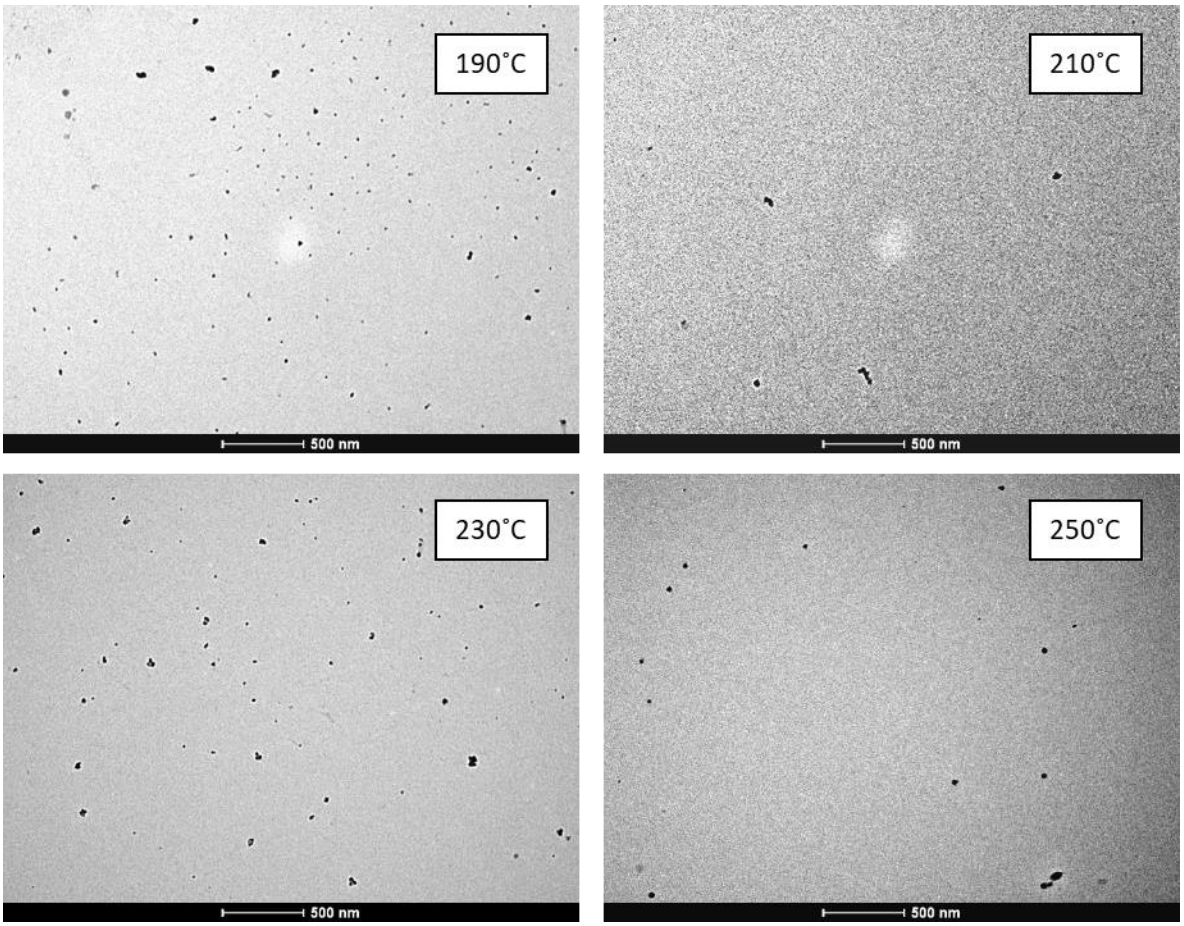

Figure S6. Full-sized TEM micrographs of the fluorescent carbon nanoparticles (FCNs) prepared in this work.

Dynamic Light Scattering

Dynamic Light Scattering (DLS) was attempted to confirm the particle size distribution of the particles. Freeze dried particles were suspended in deionized water at concentrations ranging from 0.25 mg/mL to 10 mg/mL and tested in triplicate. It was found that there was insufficient scattering for the correlogram to be constructed as expected where the y-intercept approaches ~1 (see Figure S6). Moreover, there was significant variability between repeat runs, underlining the poor quality of the light scattering. This was likely due to the high absorption of the samples; automatically selected attenuation was consistently 10 or above. Sonication did not result in consistent data. Nor did performing DLS prior to freeze drying.

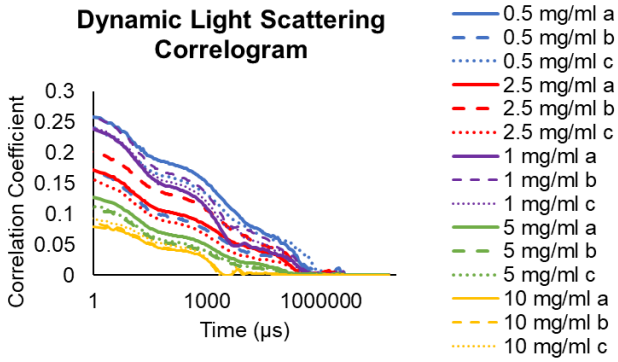

Figure S6. Dynamic Light Scattering correlogram. Triplicate measurements were attempted, labeled as a, b, and c. Increasing the concentration of the analyzed sample did not increase the observed scattered intensity, likely indicating strong sample absorbance. Because these samples were unfortunately not able to be measured, ζ-potential measurements were not collected. However, previous examination of this FCN formulation have revealed them to be near-neutral.[1,6]

<u>UV-Vis and fluorescence spectral data</u>

Top reading absorbance and fluorescence measurements were taken in Greiner UV-Star® flat bottom 96 well plates with 200 µL present in each well using a TECAN Infinite® M1000 PRO Microplate Reader (Männdorf, Switzerland). Fluorescence excitation and emission scans were performed to reveal peak excitation of 376 nm and emission at 466 nm (see Figure S8).

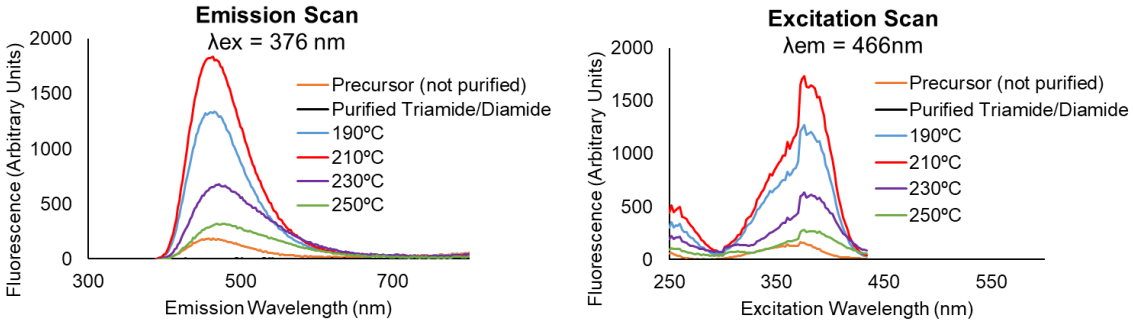

Figure S8 - Fluorescence spectra of precursor, purified diamide/triamide product, and particles pyrolyzed at various temperatures at a concentration of 0.05 mg/mL in water. Emission scan (left) and excitation scan (right).

The peak fluorescence was plotted as a function of concentration as shown in Figure S9. The relationship was close to linear for the entire concentration range analyzed, though the higher pyrolysis temperatures appear to deviate slightly from linearity above approximately 0.05 mg/mL. Therefore, concentrations below 0.05 mg/mL are considered to be safely within the linear range.

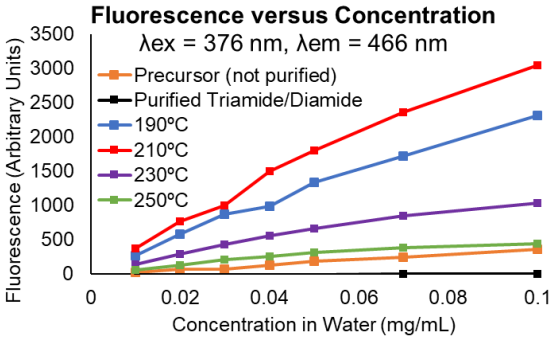

Figure S9 - Fluorescence of precursor, purified diamide/triamide product, and particles pyrolyzed at various temperatures as a function of concentration

FTIR

Fourier Transform Infrared Spectroscopy (FTIR) was used to identify functional groups present in the particles and precursor. The spectra were obtained using a Nicolet™ iS50 FTIR Spectrometer equipped with Attenuated Total Reflection capabilities. The particles/precursor were not suspended in any solvent.

The results are shown in Figure S10. The peaks show the presence of amide groups (peaks at 1692, 1636, and 1540 cm^{-1}, indicated by solid grey lines). There is a very small peak at 1776 cm^{-1} indicating the presence of interchain imide bonds on all samples excluding the precursor (dashed grey line). The FTIR results were not able to show statistically significant differences between the particles pyrolyzed at different temperatures.

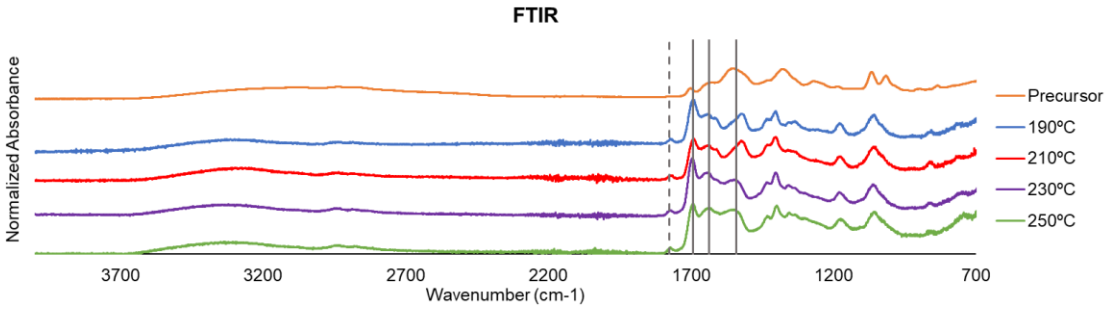

Figure S10 - FTIR results for precursor and particles pyrolyzed at various temperatures. Spectra are normalized and y-shifted for clarity. Peaks at 1692, 1636, and 1540 cm^{-1} correspond to amide groups (indicated by solid grey lines). There is a small peak for the four pyrolyzed particles at 1776 cm^{-1} corresponding to interchain imide groups (dashed grey line).

XPS

At the Cornell Center for Materials Research (CCMR), X-ray Photoelectron Spectroscopy (XPS) measurements were collected using a Scienta Omicron ESCA-2SR with operating pressure ca. $1x10^{-9}$ mBar. Monochromatic Al Kα X-rays (1486.6 eV) were generated at 300 W (15 kV; 20 mA). Analysis spot size was 2 mm in diameter with a 0° photoemission angle and a source to analyzer angle of 54.7°. A hemispherical analyzer determined electron kinetic energy, using a pass energy of 200 eV for wide/survey and 50 eV for high resolution scans. A low energy electron flood gun was used for charge neutralization of non-conductive samples.

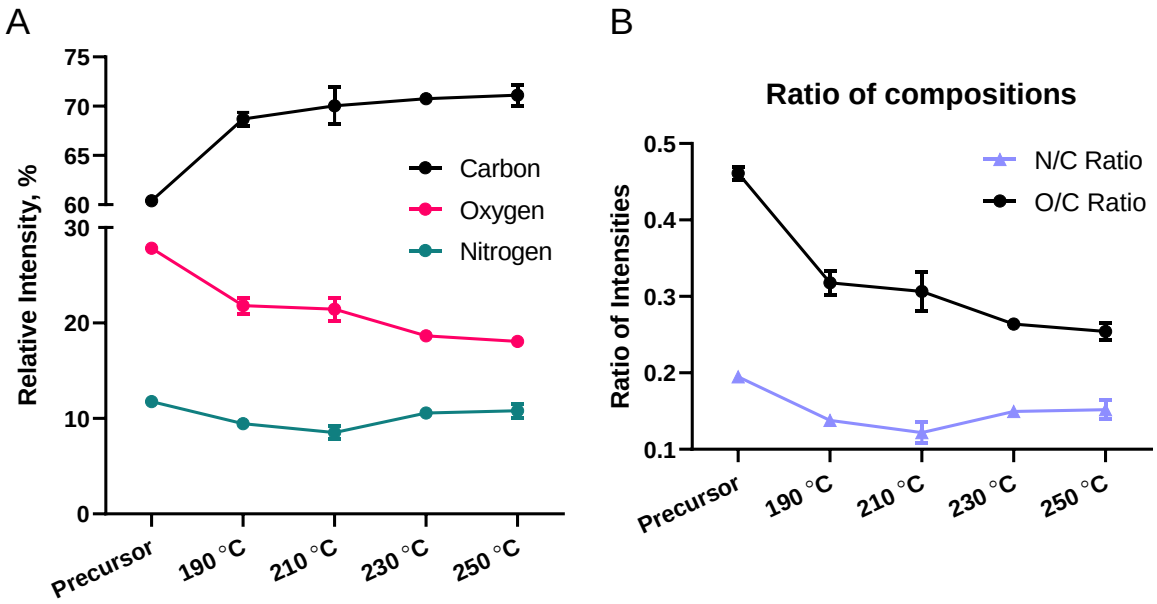

Figure S11 – A. Elemental composition from XPS survey spectra of carbon, oxygen, and nitrogen present in the precursor and FCNs. **B.** The oxygen to carbon and **C.** nitrogen to carbon ratio from the survey data.

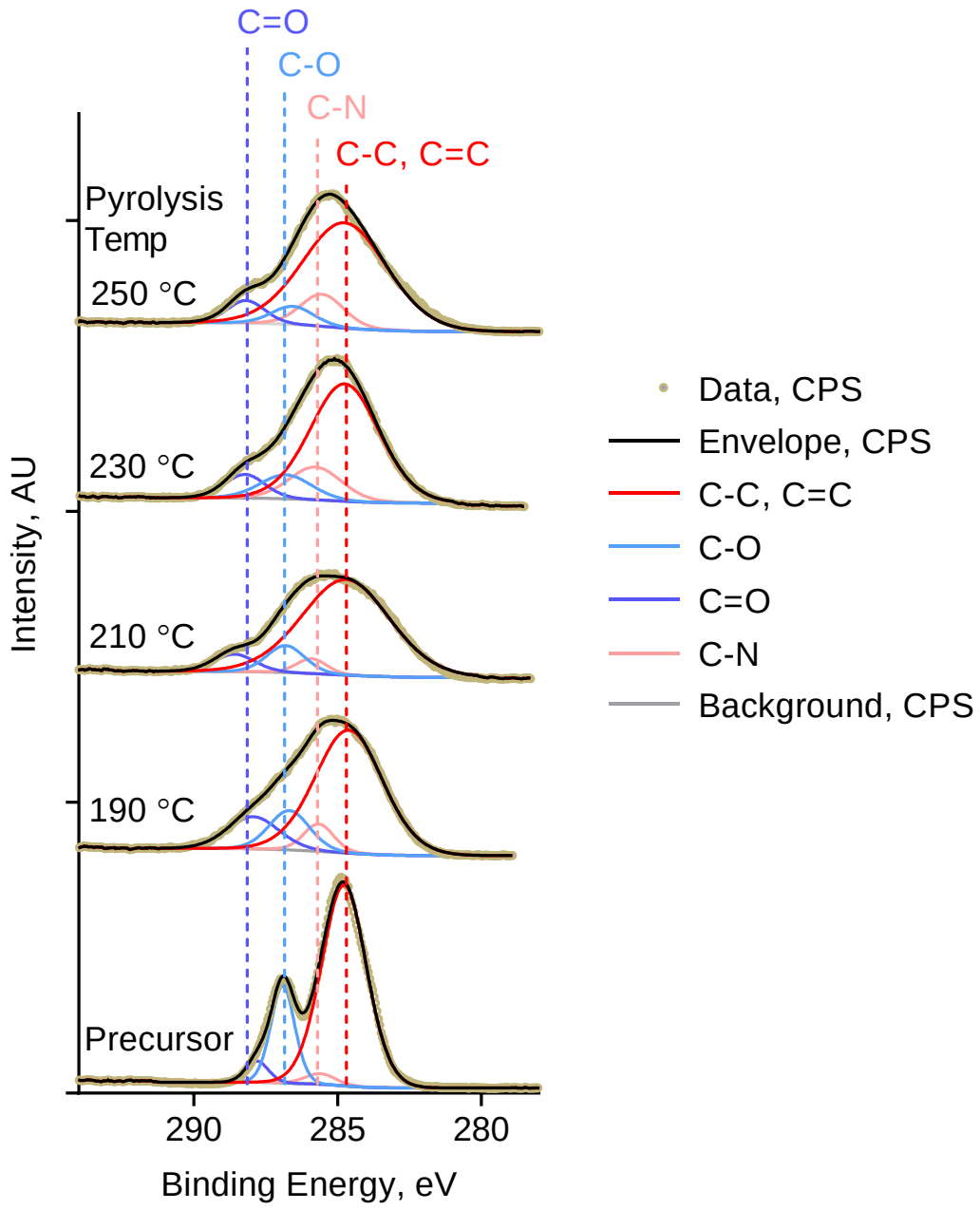

Figure S12 – C 1s XPS spectra of FCNs and precursor. Voigt profiles were centered and fit at carbon components representing general C=C/C-C, C-N (includes all amines, excludes amides), C-O (includes C-OH and C-O-C), and C=O (amide, ketones, etc.) bonds. From 190-250 ˚C, the consistent reduction in C-O matches with the consistent reduction in oxygen content observed in the survey.

QCM-D

Quartz Crystal Microbalance with Dissipation (QCM-D) experiments were repeated with a variety of particle concentrations. The results are shown in Figure S13. Particle adsorption increased with particle concentration in a nonlinear manner. Particle desorption was minimal.

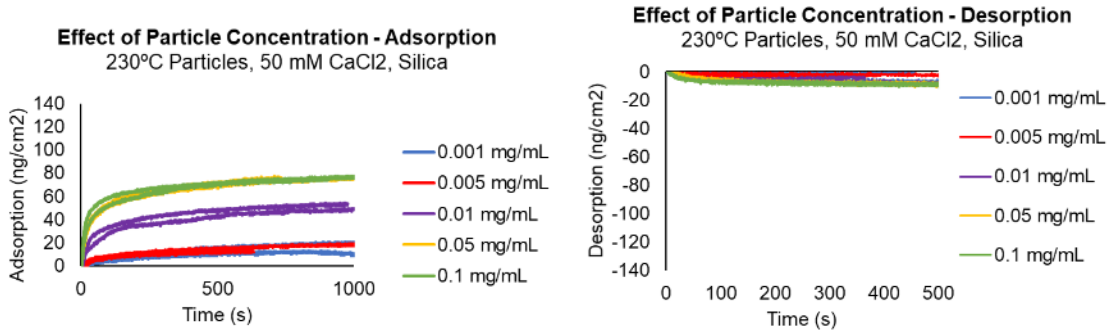

Figure S73 - Adsorption (loading) and desorption (flushing) of particles pyrolyzed at 230 ˚C at different particle concentrations. Note the different y and x axis scales.

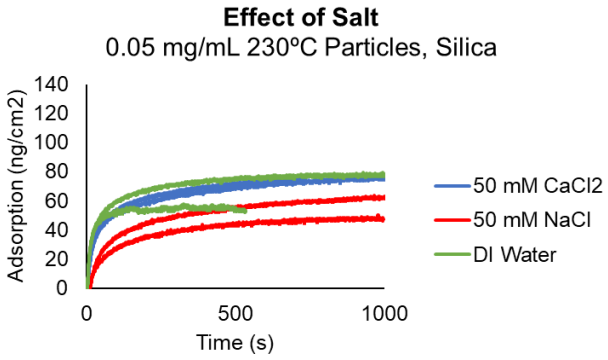

Figure S84 – QCM-D results showing effect of salt concentration on adsorption of 230 ˚C particles

The type of salt in the QCM-D solution was varied to test the effect on adsorption. The blank solutions in the three cases were 50 mM $CaCl_2$, 50 mM NaCl, and deionized water. The blank solution was introduced until the system was stable as described in the Main Text. 230 ˚C particles at a concentration of 0.05 mg/mL in 50 mM $CaCl_2$, 50 mM NaCl, or deionized water was then introduced until adsorption reached a plateau, and then the baseline solution was re-introduced. It was found that the presence of a divalent salt at 50 mM did not have a statistically significant effect on adsorption relative to the replication error (Figure S14) . NaCl

showed only a minor decrease in retention relative to the replication uncertainty. This is in agreement with a hydrophobic adsorption mechanism, where salt would not be expected to have a significant effect.

Contact Angle of QCM-D Chip Surfaces

The contact angle measurements of QCM-D chips were completed using a Ramé-Hart Instrument Co Model 250-F1 goniometer, Ace I light source, a PixeLINK camera, and 2 µL of water from a Gilmont Instruments GS-1200 syringe. Images were taken in triplicate (n=3) in PixeLINK Capture OEM and analyzed in DROPimage Advanced. Measurements are reported as average ± standard deviation. The Fe_2O_3 surface had a contact angle of 56.6 ± 0.25 degrees, the SiO_2 surface had a contact angle of 23.7 ± 2.25 degrees, and the AlSiO surface had a contact angle of 14.7 ± 3.85 degrees.

References

(1) Li, Y. V.; Cathles, L. M.; Archer, L. A. Nanoparticle Tracers in Calcium Carbonate Porous Media. *J. Nanoparticle Res.* **2014**, *16* (8). https://doi.org/10.1007/s11051-014-2541-9.

(2) Krysmann, M. J.; Kelarakis, A.; Dallas, P.; Giannelis, E. P. Formation Mechanism of Carbogenic Nanoparticles with Dual Photoluminescence Emission. *J. Am. Chem. Soc.* **2012**, *134* (2), 747–750. https://doi.org/10.1021/ja204661r.

(3) Song, Y.; Zhu, S.; Zhang, S.; Fu, Y.; Wang, L.; Zhao, X.; Yang, B. Investigation from Chemical Structure to Photoluminescent Mechanism: A Type of Carbon Dots from the Pyrolysis of Citric Acid and an Amine. *J. Mater. Chem. C* **2015**, *3* (23), 5976–5984. https://doi.org/10.1039/c5tc00813a.

(4) Schneider, J.; Reckmeier, C. J.; Xiong, Y.; Von Seckendorff, M.; Susha, A. S.; Kasak, P.; Rogach, A. L. Molecular Fluorescence in Citric Acid-Based Carbon Dots. *J. Phys. Chem. C* **2017**, *121* (3), 2014–2022. https://doi.org/10.1021/acs.jpcc.6b12519.

(5) Fang, Q.; Dong, Y.; Chen, Y.; Lu, C. H.; Chi, Y.; Yang, H. H.; Yu, T. Luminescence Origin of Carbon Based Dots Obtained from Citric Acid and Amino Group-Containing Molecules. *Carbon N. Y.* **2017**, *118*, 319–326. https://doi.org/10.1016/j.carbon.2017.03.061.

(6) Subramanian, K.; Yan Li, S.; Cathles, L. M. Assessing Preferential Flow by Simultaneously Injecting Nanoparticle and Chemical Tracers. *Water Resour. Res.* **2013**, *49* (1), 29–42. https://doi.org/10.1029/2012WR012148.